Fusion Engineering and Design 88 (2013) 940–944

Contents lists available at ScienceDirect

Fusion Engineering and Design

journal homepage: www.elsevier.com/locate/fusengdes

RF optimisation of the port plug layout and performance assessment of the ITER ICRF antenna

M. Vrancken[a,*], F. Durodié[a], R. Bamber[b], N. Dalton[b], P. Dumortier[a], M. Graham[b], A. Horvat[b], D. Hancock[b], D. Lockley[b], F. Louche[a], R. Maggiora[c], A. Messiaen[a], D. Milanesio[c], M.P.S. Nightingale[b], M. Shannon[b], P. Tigwell[b], M. Van Schoor[a], D. Wilson[b], K. Winkler[d], Cycle Team[a,b,c,d,e]

[a] ERM-KMS, Association EURATOM-Belgian State, Brussels, Belgium
[b] EURATOM/CCFE Association, Culham Science Centre, Abingdon OX14 3DB, United Kingdom
[c] Associazione EURATOM-ENEA, Politecnico di Torino, Torino, Italy
[d] IPP-MPI, EURATOM-Assoziation, Garching, Germany
[e] Association EURATOM-CEA, DSM/IRFM, Cadarache, France

ARTICLE INFO

Article history:
Available online 22 March 2013

Keywords:
Plasma heating
ICRF
Antenna
ITER

ABSTRACT

The ITER Ion Cyclotron Range of Frequencies (ICRF) antenna's capacity to couple power to plasma is determined by the plasma Scrape-Off Layer (SOL) profile, shaping of the front strap array, layout of the Port Plug (PP) and detailed design of its RF components. The first two factors are taken into account by the Torino Polytechnic Ion Cyclotron Antenna (TOPICA) calculated strap array Scattering/Impedance 24-port ($S_{24\times24}-/Z_{24\times24}-$) matrices, while this paper deals with the optimisation of the PP layout and components. The RF modeling techniques are explained and used to maximise the coupled power under a set of constraints on RF quantities inside the PP. The total PP RF surface conductive and volumetric dielectric losses are calculated. The resulting *S*-parameters at the rear RF PP flanges are evaluated as input for the design of the pre-match, decoupling and matching network outside the PP. A discussion of the effect of errors on the PP excitation on the coupled power is also included.

1. Introduction

This paper assesses the RF performance of the present status (Section 2) of the design for the ITER ICRF antenna. Section 3 describes the full antenna array and PP RF model used to optimise the coupled power over the 40–55 MHz frequency band under a set of limitations on RF quantities inside the PP. The resulting coupled power characteristic of Section 4 shows a sharp drop in performance at higher frequency as limited by the 4-port junction (4PJ see Fig. 1) contact current I_J and Service Stub (SS) voltage V_{SS}. A 1 MHz margin over 55 MHz is provided for the triplet current poloidal $\phi = (0,-\pi/2)$ and $\theta = (0,\pi,0,\pi)$ toroidal phasing as indicated in Fig. 6. Section 5 shows the 3D evaluation of the 4PJ RF electric fields. Section 6 evaluates the total PP RF surface conductive and volumetric dielectric losses at 1.12 MW. The evaluation of the PP RF flange $S_{8\times8}$-parameters in Section 7 leads to a final discussion in Section 8 on the accuracy required for the PP excitation realised by the decoupling- and matching network [1] to achieve the predicted coupled power performance.

2. Status port plug RVTL layout

Fig. 1 shows a CAD cross section along a lower inner 4PJ and Removable Vacuum Transmission Line (RVTL) central axis, with as main parameters: the 4PJ length L_J, the distance from 4PJ back to T-point L_{JT}, the Service Stub (SS) length L_{SS}, and the position of the front and rear Vacuum Ceramic Windows (VCWs) L_{1T} and L_{T2}. The radial available length $L_{A1} - (L_J + L_{JT})$ for fitting the SS is smaller than the required $\sim\lambda_{midband}/4$, leading to an inward folded construction of length L_{fold}. Modifications since [2] have followed the evolution to the present strap array front face geometry. A neutron shield with characteristic impedance 15 Ω was introduced to block a direct line of sight from plasma along the 4PJ side to the front VCW ceramic. The shape of the rear 4PJ creates an asymmetric current density J_S [A/m] which can cause overheating in the individual fingers of the sliding RF contact, which is relocated inside a coaxial insert of length l_{insert} = 120 mm to smoothen J_S sufficiently. A double round-off radius on the coax insert outer tip and shaping of 4PJ housing were required for E-field control as shown in Fig. 5. Additional

* Corresponding author. Tel.: +32 0044(0)1235466772.
E-mail address: Mark.Vrancken@ccfe.ac.uk (M. Vrancken).

0920-3796/$ – see front matter
http://dx.doi.org/10.1016/j.fusengdes.2013.02.162

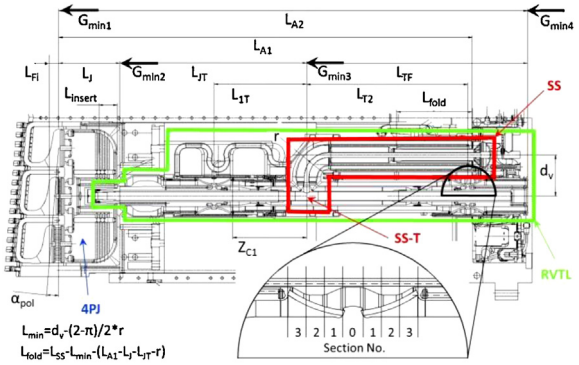

Fig. 1. Cross section through lower inner (1/8) module of ITER ICRF Antenna with 4-port junction (4PJ), Removeable Vacuum Transmission Line (RVTL), Service Stub (SS), T-point (SS-T), front "25 Ω" VCW, zoom on proposed rear "20 Ω" VCW and physical lengths L_{A1} = 2722, L_{A2} = 3086, L_J = 403, L_{JT} = 1229, L_{1T} = 609, L_{T2} = 1061, d_v = 207, r = 144, L_{SS} = 1795, L_{fold} = 497 (all dimensions in [mm]).

modifications not affecting the overall layout are discussed in Section 4.

3. Full antenna array and port plug RF model

The total RF model is shown in Fig. 2. The TOPICA [3] $S_{24\times24}$ matrix takes into account the front strap array geometry and the "low density" plasma SOL profile provided by ITER Organisation (April 2010) [4]. The 4PJs are incorporated using MWS [5] $S^{U}_{4\times4}$, $S^{L}_{4\times4}$ matrices (different α_{pol} affecting feeder lengths l_{Fi}). The 8 identical RVTLs are modeled with $S_{2\times2}$ matrices determined by a multi-section Transmission Line (TML) model, each section characterised by an electrical length $l_i = L_i - \Delta l_i$, characteristic impedance Z_{ci}, and ratio of local phase velocity to speed of light v_{fi}/c_0 (example in Table 1), all determined by error minimisation between S-parameters of subcomponent 3D MWS models and multi-section TML models. The circuit model is excited by the complex forward voltages V_8^{F+} at the PP RF flanges, such that the voltage maxima V_8^{max} on the 20 Ω Main Transmission Lines (MTL), positioned near the decoupler- and matching network outputs A–H by the phase shifter lengths l_8, have the ideal set of (ϕ,θ) phasings [1]. The pre-matching networks are assumed to be set identical.

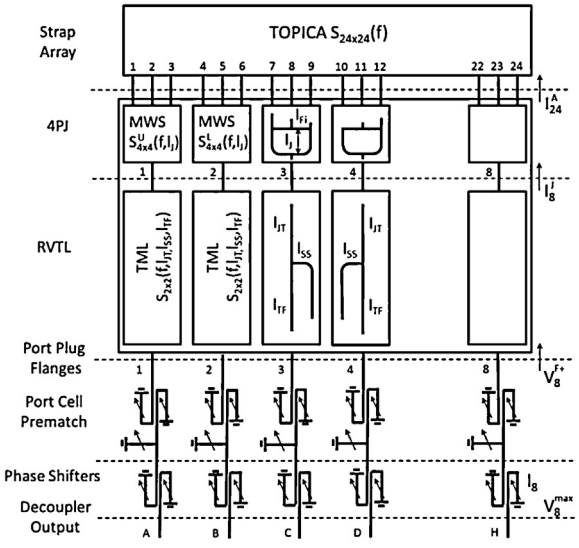

Fig. 2. Total port plug RF circuit, with antenna array $S_{24\times24}$, 4PJ $S_{4\times4}$ and RVTL $S_{2\times2}$ scattering matrices to obtain the PP RF flange $S_{8\times8}$, with electrical length corrections Δl_{SS} = 0.070, $\Delta L_{JT} = \Delta l_{TF}$ = 0.004 applied around the SS T-point.

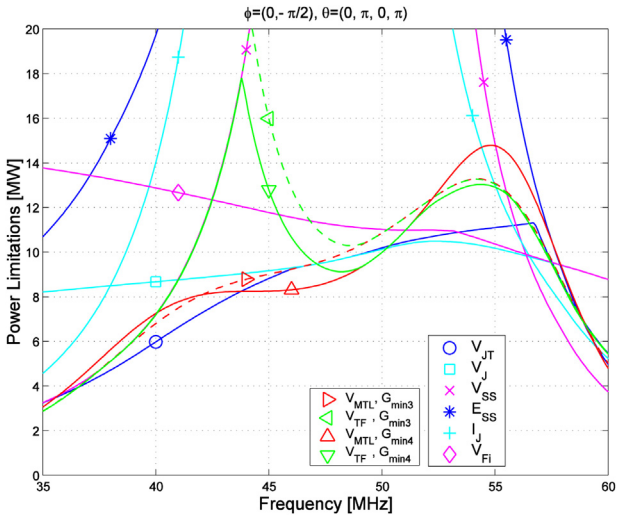

Fig. 3. The total coupled power by the antenna array is limited by RF quantities inside the PP (V_{max} = 45 kV, E_{SS} = 3 kV/mm, I_J = 2 kA) to the "lower envelope" of the set of curves shown. The V_{TF} and V_{MTL} limitations at the SS T-point $P_c = 1/2G_{min3}V^2_{max}$ and at the PP rear flange $P_c = 1/2G_{min4}V^2_{max}$ are compared.

4. Optimisation of coupled power

For each frequency, (ϕ,θ) phasing, and set of RVTL layout parameters, the RF quantities on strap feeders, 4PJs and RVTLs are calculated and limited to V_{max} = 45 kV, E_{SS} = 3 kV/mm (electric field at SS fold) and 4PJ contact current I_J = 2.0 kA as shown in Fig. 3. The "lower envelope" is the coupled power P_c if all limitations are respected. The maximum installed generator power is 24 MW [6]. The shape of this graph and the position of the sharp fall off above 55 MHz are controlled by choosing L_J, L_{JT} and L_{SS}. The dependence of the coupled power level on the SOL profile is examined in [7] while an increase of coupled power with a poloidal array phasing $\phi = (0,\pi)$ [2] is possible at the cost of increased complexity in the feed network [8]. Fig. 3 compares the responses at the SS T-point connections to the straight lines ($P_c = 1/2G_{min3}V^2_{max}$, front 25 Ω VCW and 20 Ω MTLs from T-point) and the PP flanges ($P_c = 1/2G_{min4}V^2_{max}$, front/rear 25 Ω/25 Ω VCWs), with G_{min} the array effective minimum conductance at that position (see Fig. 1), a generalisation of the 1-port relation $G_{min} = 1/Z_C(1-|S_{11}|)/(1+|S_{11}|)$. When using a 25 Ω rear VCW, it affects the standing wave pattern giving the G_{min4} response of Fig. 4, potentially leading to 10% reduction (midband 43–50 MHz) in coupled power. Although the main ITER ICRF schemes are concentrated near the band edges (40–45, 50–55 MHz [9]), two sets of modifications are presently evaluated: 1. The rear VCW cross section is modified as in Fig. 1 to bring the equivalent impedance Z_{ci} closer to the ideal 20 Ω case (see Table 1). Fig. 4 shows that the midband performance recovery is not complete as the improvement in impedance is limited by the electric field inside the modified VCW. The high frequency margin is not affected. 2. Use two identical VCWs, make L_{SS} = 1.735 m and modify Z_{c1} (between front VCW and T-point, see Fig. 1) to 22 Ω (d_a = 127.5 m) instead of Z_{c1} = 20 Ω (d_a = 132.5 mm, d_b = 185.0 mm). This recovers the midband performance, but some loss on the coupling of the phasings with highest coupling is observed. The high frequency margin of the $\theta = (0,\pi,0,\pi)$ phasing for the front/rear = 25 Ω/25 Ω case is 0.3 MHz lower than the 56.4 MHz for the other cases, still leaving a ~1 MHz design margin.

5. 4-Port junction electric field analysis

All RF surfaces were dimensioned to satisfy the $|E_{//}| < 2$ kV/mm, $|E_{\perp}| < 3$ kV/mm torus and $|E_{//}| < 3$ kV/mm, $|E_{\perp}| < 3$ kV/mm private

Table 1
Equivalent TML model parameters for original "25 Ω" and proposed modified "20 Ω" VCW.

		"25 Ω" window VCW			Modified "20 Ω" VCW		
Section no.	0	1	2	3	1	2	3
L_i [m]	0.035	0.031	0.031	0.031	0.031	0.031	0.031
Z_{ci} [Ω]	20.00	26.44	25.37	24.82	24.57	20.76	20.14
v_{fi}/c_0	1.00	0.765	0.781	0.788	0.789	0.775	0.786

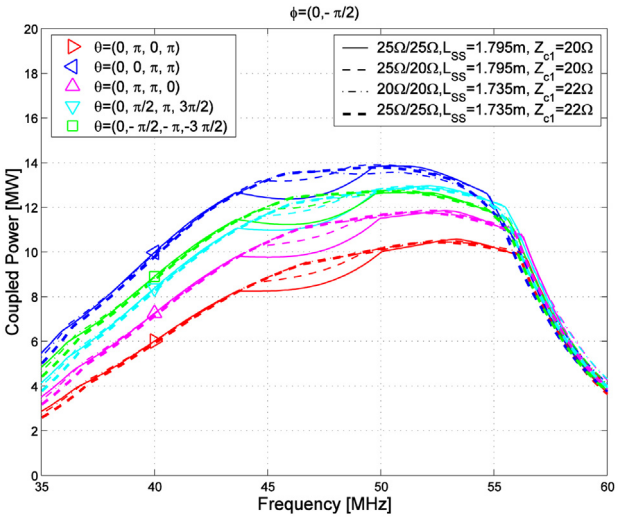

Fig. 4. The total coupled power by the antenna array for (strap feeder) poloidal $\phi=(0,-\pi/2)$ phasing as a function of frequency for different toroidal phasings, comparing combinations of front/rear "25 Ω" and "20 Ω" VCWs (see Table 1) and different L_{SS} and Z_{c1}.

vacuum constraints [10]. Analytical formulas and the 2D planar/axi-symmetric electrostatic field solver FEMM [11] were used to dimension gaps and round-off radii. Subsequently, MWS 3D RF analysis was used to verify the electric field levels, as in Fig. 5 for the 4PJ inner reaching 45 kV at 53 MHz (see Fig. 3). In Fig. 5(a), the total field is maximum on the top/bottom and back of the 4PJ approaching 2.8 kV/mm. In Fig. 5(b) the $|E_{//}|$-field remains <2 kV/mm over most of the 4PJ inner, but reaches ~2 kV/mm on the top/bottom edges, due to an increase of the RF voltage over the height of the junction. Inaccuracies in the 3D E-field levels remain because the voltage inside the MWS 4PJ is estimated assuming a single TML with $Z_{ci}=4.47\ \Omega$, the splitting of the model at strap and 4PJ feeders (see Fig. 2) (non-TEM fields), and the difference in loading between a MWS vacuum loaded single triplet and plasma loaded full array TOPICA models.

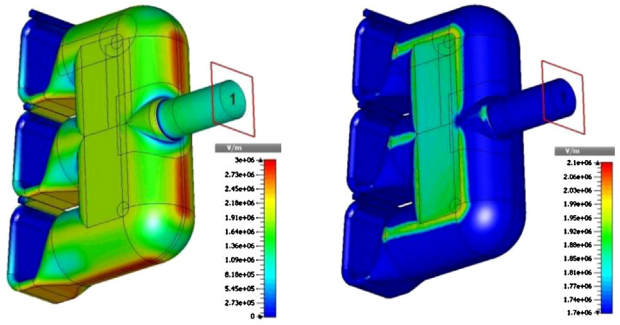

(a) (b)

Fig. 5. (a) Total electric field $|E|$ from 0–3.0 kV/mm and (b) parallel electric field $|E_{//}|$ from 1.7 to 2.1 kV/mm on inner 4PJ at 53 MHz.

6. RF resistive and dielectric loss evaluation

RF surface resistive losses for non-coaxial components are evaluated from 3D MWS models (see Fig. 5) according to

$$P_{R,MWS} = \frac{1}{2}\int_S R_{S,metal}(f,T)\cdot|J_S(f)|^2\cdot dS \quad (1)$$

with surface resistance $R_{S,metal}(f,T)=\sqrt{\pi\mu_0\rho_{metal}(T)}$. The resistivity ρ_{metal} for each metal (Be, CuCrZ, Cu, SS316L, In718) depends on temperature T and irradiation damage (when data available [12]) and the surface current $J_S(f)$ is scaled to the correct frequency and amplitude from the RF circuit model. Resistive losses for coaxial components are evaluated from

$$P_{R,TML} = \frac{1}{2}\frac{1}{\pi d_i}\int_l R_{S,metal}(f,T)\cdot|I(f,z)|^2\cdot dz \quad (2)$$

with inner and outer diameters d_a, d_b by integration of the standing current wave pattern $I(f,z)$ from the RF circuit simulation. These estimates rely on the low conductivity of pure electrodeposited Cu, only achieved in reality with strict control over the plating process [13]. Front and rear VCWvolume dielectric losses are evaluated from 3D MWS models as

$$P_{D,MWS} = \frac{1}{2}\int_v \sigma_D(f)\cdot|E_D(f,z)|^2\cdot dV \quad (3)$$

with the frequency dependent dielectric losses modeled as $\sigma_D(f)=2\pi\in_o\in_r tan\,\delta$ with $\varepsilon_r=9.95$ and loss tangent $\tan\delta=3.0e{-}4$ for a high purity (96.5–99%) irradiated Alumina at 300 °C [14]. The MWS field $E_D(f,z)$ inside the ceramic cones is scaled to the operating voltage in the standing wave pattern $V(f,z)$ from the RF circuit simulation. Table 2 gives an overview of losses at a discrete set of frequencies per component, for one triplet and the full PP, resulting in a maximum estimate of 1.12 MW at 55 MHz.

7. Rear port plug RF flange *S*-parameters

A given RVTL layout transforms the TOPICA $S_{24\times24}$ matrix into the rear PP RF flange $S_{8\times8}$ matrix which is the starting point to design the pre-match, decoupling and matching network. Fig. 6 shows that the frequencies where the magnitude of the diagonal *S*-parameter elements are small correspond to the highest coupled power in Fig. 3. Fig. 7 shows that the present RVTL optimisation (G_{min4} case) also results in higher mutual coupling at the higher edge of the frequency band, somewhat mitigated by the proposed modifications of Section 4, relaxing the tunable element specifications in the decoupler- and matching network [8].

8. Sensitivity to feed network excitation errors

The effect of a finite precision on the excitations V_8^{max}, V_8^{F+} on the coupled power curves is studied by adding absolute phase and relative amplitude errors $\Delta\varphi_a$, ΔA_r as

$$V_i' = V_i(1+(\pm1)_{Ai}\cdot\Delta A_r)\cdot\exp(j(\pm1)_{\varphi i}\cdot\Delta\varphi_a) \quad (4)$$

and iterating each calculated point N_e times with sets of randomly generated signs $(\pm1)_{Ai=1,\ldots,8}$, $(\pm1)_{i\varphi=1,\ldots,8}$ to achieve convergence

Table 2
Summary of RF losses for a single triplet and the full PP at discrete set of frequencies and elevated temperature (200 °C/300 °C).

RF losses [kW]	T [°C]	Loss frequency [MHz]				
Component		40	43	47.5	53	55
Faraday screen						
FS frames	300	3.4	3.9	4.4	4.4	4.0
FS bars	300	9.4	11.0	12.3	12.1	11.1
FS supports	300	3.0	3.5	4.0	4.0	3.7
Triplet straps						
3xstrap	300	16.2	18.5	20.2	19.2	17.5
Triplet housing						
Inner	200	4.0	4.5	4.7	4.2	3.7
Outer	200	1.1	1.6	1.5	1.8	1.9
4-Port junction						
Inner	200	2.3	1.9	1.4	2.1	2.8
Outer	200	1.5	1.1	0.7	1.3	1.9
Removable Vacuum Transmission Line (4PJ back to PP flange)						
Inners	200	38.0	36.3	27.8	47.5	53.3
Outers	200	28.6	26.8	19.9	35.2	39.6
VCW dielectric losses						
Front	200	0.65	0.67	0.46	0.24	0.04
Rear	200	0.09	0.14	0.69	0.80	0.51
(Sub)Total						
1 triplet		108	110	98	133	140
8 triplets		866	878	783	1062	1121

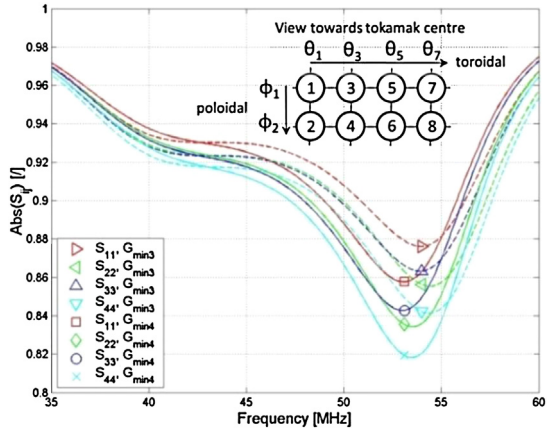

Fig. 6. Amplitude of diagonal elements of $S_{8\times8}$ (normalised to 20 Ω) over 35–60 MHz at the SS T-points (G_{min3}) and PP flanges (G_{min4}).

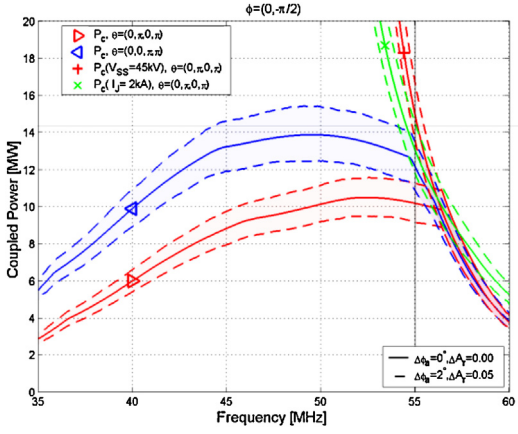

Fig. 8. Investigation of (absolute) phase $\Delta\varphi_a$ and (relative) amplitude ΔA_r errors on the PP excitation voltages V_8^{F+}, V_8^{max} on coupled power performance ($P_c = 1/2G_{min3}V_{max}^2$) and I_J and V_{SS} limiting curves.

to the worst possible combination of errors. Fig. 8 shows that for $\Delta\varphi_a = 2°$, $\Delta A_r = 5\%$, with small $\Delta\varphi_a$ and low mutual coupling, the error is dominated by ΔA_r and would result in a 10% shift in coupled power. The downward shift of the steep V_{SS} limitation hardly affects the high frequency margin, while the upward shift of the I_J limitation needs special care as an I_J underestimate can result in catastrophic damage to the RF sliding contact, while V_J, V_{SS} underestimates will manifest itself as arcing/generator tripping. As experienced with the JET ITER-Like Antenna [15], a more accurate direct control over the front strap array current spectrum could be achieved by incorporating measurements closer to the straps ($V+I$-probes behind 4PJ) into the control system.

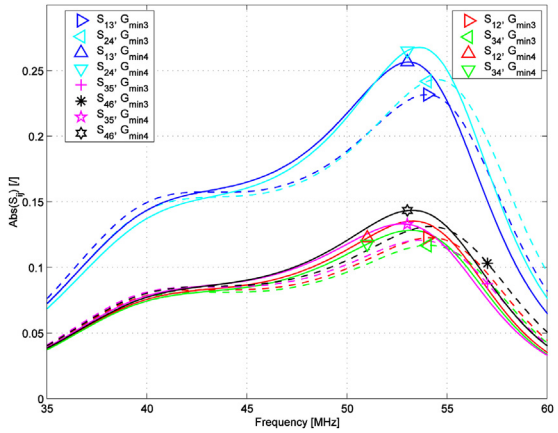

Fig. 7. Amplitude of main poloidal and toroidal cross coupling S-parameters (normalised to 20 Ω) over 35–60 MHz as seen at the SS T-points (G_{min3}) and PP flange positions (G_{min4}).

9. Conclusions

The strap array and PP layout have been optimised to maximise the coupled power for the 2010 "low density" plasma SOL profile, considered a pessimistic case which might improve with future SOL re-evaluations, or by moving the antenna (1 cm) forward. The coupled power falls off sharply above 55 MHz with a margin of ~1 MHz to safeguard against uncertainty on the RF contact current ($I_J = 2.0$ kA), the VCW characteristics (both proposed R&D) and the accuracy of the PP excitation. Overall RF losses are estimated at 1.12 MW, provided a high quality plating process can be achieved. Another R&D proposal will verify strap, 4PJ and RVTL geometry on a full scale ¼ antenna low power mock-up by S-parameter

measurement and the calculated coupled power limiting curves with independent RF diagnostics ($V+I$ probes, I-coils) inside the RVTL.

Acknowledgments

The project F4E-2009-GRT-026 has been funded with support from Fusion for Energy. The views and opinions expressed herein do not necessary reflect those of Fusion For Energy or European Commission or ITER Organisation. Fusion For Energy is not liable for the use which might be made of the information in this publication.

References

[1] A. Messiaen, R. Koch, R. Weynants, P. Dumortier, F. Louche, R. Maggiora, et al., Performance of the ITER ICRF system as expected from TOPICA and ANTITER II modelling, Nuclear Fusion 50 (2010) 1–21.
[2] M. Vrancken, F. Durodie, P. Dumortier, D. Lockley, F. Louche, A. Messiaen, et al., Optimization of the layout of the ITER ICRF antenna Port Plug and its performance assessment, in: 19th Top. Conf. RF Power in Plasmas, Newport, RI, USA, 2011, pp. 62–64.
[3] D. Milanesio, R. Maggiora, ITER ICRF antenna analysis and optimisation using the TOPICA Code, Fusion Engineering and Design 50 (2010) 1–10.
[4] ITER Organisation, ITER Organisation Scrape Off Layer Profiles, 2010. Available from: IDM ref https://user.iter.org/?uid=33Y59M&version=v2.3
[5] MWS, CST GmbH, CST Microwave Studio, Company Webpage, 2012. http://www.cst.com/content/products/mws/overview.aspx
[6] P. Lamalle, P. Lamalle, B. Beaumont, F. Kazarian, T. Gassmann, G. Agarici, et al., Status of the ITER H&CD System, SOFT, Liege, Belgium, 2012.
[7] A. Messiaen, R. Weynants, ICRH antenna coupling physics and optimum plasma edge density profile. Application to ITER, Plasma Physics and Controlled Fusion 53 (2011) 085020.
[8] M. Vervier, A. Messiaen, P. Dumortier, Alternative Proposals for the ITER ICRH Decoupling and Matching System, SOFT, Liege, Belgium, 2012.
[9] M.-L. Mayoral, L. Colas, L.G. Eriksson, M. Graham, P. Jacquet, E. Lerche, et al., ICRF Heating at JET: from Operation with a Metallic Wall to the long term perspective of a DT campaign, in: 19th Top. Conf. RF Power in Plasmas, Newport, RI, USA, 2011, pp. 253–256.
[10] ITER Organisation, ITER Design Review – Answer to Chit #04, 2010. Available from: https://user.iter.org/?uid=3XWCT9
[11] FEMM, Finite Elements Method Magnetics, 2012. Available from: http://www.femm.info/wiki/HomePage
[12] ITER Organisation, ITER Document No. G 74 MA 16, CuCrZr, Irradiated, Electrical Resisitivity, 2012. Available from: https://user.iter.org/?uid=256NYW&action=get_document
[13] A. Fowler, Radio frequency performance of electroplated finishes, in: Proceedings of I.R.E.E. Australia, 1970, pp. 148–164.
[14] R. Bamber, An Investigation into the Effects of Changing Loss Tangent, Culham Centre Fusion Energy, Abingdon, UK, 2010.
[15] F. Durodie, M. Nightingale, M.-L. Mayoral, J. Ongena, A. Argouarch, G. Berger-By, et al., Physics and engineering results obtained with the ion cyclotron range of frequencies ITER-like antenna on JET, Plasma Physics and Controlled Fusion 54 (2012) 1–16.